ORIGINAL PAPER

RJME Romanian Journal of Morphology & Embryology http://www.rjme.ro/

QuPath-assisted digital quantification of CD20, CD3 and BCL2 in mature B-cell lymphoid neoplasms: a single-center exploratory study

PAUL-CĂTĂLIN TOBOLTOC[1,2)]

[1)]*Department of Pathology, Sibiu Emergency County Clinical Hospital, Sibiu, Romania*

[2)]*Doctoral School of Medicine, Institute for the Organization of Doctoral and Postdoctoral Studies, Lucian Blaga University of Sibiu, Romania*

Abstract

Background: Mature B-cell lymphoid neoplasms require integrated morphological and immunohistochemical assessment. *Aim*: To characterize digitally quantified cluster of differentiation (CD)20-, CD3-, and B-cell lymphoma 2 (BCL2)-related profiles in a Romanian tertiary center, with secondary comparison across pre-pandemic, pandemic, and post-restriction intervals. *Materials and Methods*: Sixty-three newly diagnosed cases with evaluable archived diagnostic tissue were retrospectively analyzed. CD20-, CD3-, and BCL2-stained slides were assessed using a QuPath-assisted, morphology-guided, slide-adaptive workflow with a single 1 mm^2 tumor-rich region of interest per marker. Stain-vector calibration, detection and segmentation settings, scoring compartment, intensity thresholds, and object classification were defined or adjusted on a slide-specific basis, with visual verification and manual correction when required. CD20- and CD3-positive cell densities, CD20/CD3 ratio, lymphoproliferative tissue percentage, intratumoral CD20 density, BCL2-positive tumor cell proportion, and BCL2 *H*-score were evaluated primarily by histological subtype; temporal interval, vaccination status, and prior severe acute respiratory syndrome coronavirus 2 (SARS-CoV-2) infection were contextual variables. *Results*: Histological subtype was the main source of variation. Most CD20- and CD3-related variables showed no nominal temporal differences. An apparent temporal BCL2 difference was substantially attenuated in sensitivity analysis after exclusion of mantle cell lymphoma, indicating an important contribution of subtype composition. No nominal differences were detected in the highly imbalanced vaccination comparison. The higher CD20/CD3 ratio observed in five cases with documented prior coronavirus disease 2019 (COVID-19) was considered hypothesis-generating. *Conclusions*: Digital profiling was driven primarily by histological subtype, while temporal stratification provided secondary contextual information. QuPath-assisted assessment can complement a conventional review of archived lymphoma slides.

Keywords: mature B-cell lymphoid neoplasms, hematopathology, COVID-19, immunohistochemistry, digital pathology, QuPath.

Introduction

Mature B-cell lymphoid neoplasms (MBCLNs) comprise a heterogeneous group of entities defined by distinct architectural patterns, cytological features, immunophenotypic profiles, genetic backgrounds, tissue distributions, and clinical behaviors [1, 2]. In routine hematopathology, their classification depends on the integrated assessment of morphology, immunohistochemistry, tissue distribution, and clinicopathological context, with diffuse, nodular or follicular, interstitial, paratrabecular, marginal-zone-like, leukemic, and marrow-based patterns contributing to entity-level interpretation [1, 2]. This heterogeneity also extends to the tissue background and tumor microenvironment, where neoplastic B-cells coexist with variable T-cell infiltrates, stromal elements, macrophages, vascular structures, and immune-regulatory signals [3–6].

In routine hematopathology, much of this complexity is assessed qualitatively or semiquantitatively, particularly when immunohistochemical (IHC) slides are used for diagnostic confirmation, classification support, and visual estimation of tumor composition rather than for standardized quantitative comparison. Digital pathology allows the extraction of numerical information from whole-slide images and can transform routine IHC stains into analyzable tissue-level variables [7–9]. Recent diffuse large B-cell lymphoma (DLBCL) studies have emphasized the biological, prognostic, and methodological relevance of tissue heterogeneity, immune cell distribution, and digitally assessable immune-related parameters [10–12]. Within this routine-marker framework, cluster of differentiation (CD)20 can be used to approximate the CD20-positive B-cell or neoplastic compartment, CD3 estimates the accompanying T-cell infiltrate, and B-cell lymphoma 2 (BCL2) remains a clinically and biologically relevant anti-apoptotic marker with subtype-dependent interpretive implications [1–6, 12–14].

The coronavirus disease 2019 (COVID-19) pandemic created a distinct clinical and administrative context for the diagnosis and management of lymphoid neoplasms, including lymphoma. Patients with hematological malignancies and COVID-19 represented a clinically vulnerable population, with substantial mortality particularly among adults and hospitalized patients [15]. Pandemic-era studies documented diagnostic delay, altered care pathways, modified treatment strategies, and management adaptations in lymphoma populations [16–19]. Registry-based data also showed that lymphoma diagnosis patterns and stage distribution changed

This is an open-access article distributed under the terms of a Creative Commons Attribution-NonCommercial-ShareAlike 4.0 International Public License, which permits unrestricted use, adaptation, distribution and reproduction in any medium, non-commercially, provided the new creations are licensed under identical terms as the original work and the original work is properly cited.

during pandemic years, although short-term survival was not necessarily inferior to the pre-pandemic period [17].

Aim

Against this background, the aim of this study was to provide a digital histopathological (HP) and IHC characterization of MBCLNs diagnosed in a Romanian tertiary center, using routine CD20-, CD3-, and BCL2-stained slides assessed through a QuPath-assisted workflow. The primary objective was to describe and compare CD20-positive cell density, CD3-positive T-cell density, CD20/CD3 balance, lymphoproliferative tissue proportion, intratumoral CD20 density, and BCL2-related expression parameters across histological subtype groups. Specimen type was retained as an additional contextual variable. As a secondary contextual objective, the same digitally quantified parameters were evaluated across pre-pandemic, pandemic, and post-restriction administrative intervals, while documented vaccination status and documented prior severe acute respiratory syndrome coronavirus 2 (SARS-CoV-2) infection were retained only as exploratory contextual variables. The study was not designed to establish a causal relationship between the pandemic context, SARS-CoV-2 infection, vaccination, and lymphoma tissue phenotype, but to determine whether temporal stratification added descriptive information to the morphological and IHC profile of the cohort.

Materials and Methods

Study design and case selection

This retrospective observational study was conducted at the Sibiu Emergency County Clinical Hospital, Sibiu, Romania. The source population was extracted from the internal lymphoma-related pathology database and included diagnostic records generated between 11 March 2018 and 7 March 2024. The study was designed as an exploratory, single-center digital HP and IHC analysis of archived diagnostic tissue samples from MBCLNs. Temporal stratification and specimen type were retained as contextual variables, while the main analytical focus remained the quantitative assessment of routine CD20-, CD3-, and BCL2-stained slides in relation to histological subtype and digitally defined tissue compartments.

For the clinical source cohort, inclusion required a newly diagnosed MBCLN confirmed by integrated HP and IHC examination within the predefined study interval and supported by sufficient demographic, clinical, and pathological information for clinicopathological classification. For the final digital cohort, cases were additionally required to have available formalin-fixed, paraffin-embedded diagnostic tissue, corresponding Hematoxylin–Eosin (HE) sections, and evaluable CD20-, CD3-, and BCL2-stained slides suitable for whole-slide scanning, representative tumor-area selection, and quantitative image analysis. Cases were excluded from digital analysis when diagnostic tissue or corresponding IHC slides were unavailable, technically inadequate, or affected by preparation, staining, scanning, tissue-preservation, fixation-related, or sectioning artifacts that precluded reliable morphological review, region of interest (ROI) selection, and marker quantification.

For secondary contextual analysis, cases were stratified into three temporal administrative intervals: pre-pandemic, from 11 March 2018 to 10 March 2020; pandemic, from 11 March 2020, when the *World Health Organization* (WHO) characterized COVID-19 as a pandemic [20], to 8 March 2022, corresponding to the end of Romania's national state-of-alert framework [21]; and post-restriction, from 9 March 2022 to 7 March 2024, after the lifting of most COVID-19-related restrictions in Romania [22].

Clinical and pathological variables

Pathological variables recorded for all digitally evaluable cases included histological subtype, specimen type, and diagnostic tissue category. Histological subtype was established from the original diagnostic report and confirmed by review of the available HE sections and IHC profile. Specimen type was categorized according to the diagnostic material submitted for pathological examination, including lymph node samples, bone marrow biopsies, and other extranodal or tissue specimens.

Demographic and clinical variables included sex, age at diagnosis, age group, follow-up duration, and vital status at last follow-up. Documented SARS-CoV-2 vaccination before lymphoma diagnosis and tissue sampling, as well as documented SARS-CoV-2 infection before lymphoma diagnosis and tissue sampling, were recorded as temporal-context variables. For subgroup and multivariable analyses, cases were retrospectively categorized into a binary clinical-behavior group (aggressive *vs.* indolent) based on the available clinical information in the study records.

Histopathology, immunohistochemistry, and digital analysis

HP and IHC analyses were performed on formalin-fixed, paraffin-embedded biopsy or surgical specimens processed according to the routine diagnostic workflow of the Department of Pathology. HE-stained sections and the diagnostic IHC panel were reviewed for histological classification, tissue architecture, cytological features, and selection of tumor-rich areas. IHC staining was performed using the Epredia™ Autostainer 360 platform and ready-to-use Dako immunohistochemistry reagents, according to the routine laboratory protocol. The antibodies used for digital analysis were anti-CD20/CD20cy (clone L26), anti-CD3 (polyclonal rabbit anti-human), and anti-BCL2 (clone 124). Digital IHC quantification was performed on archived CD20-, CD3-, and BCL2-stained slides selected from the eligible cohort. All analyzed marker slides had been stained at the time of diagnosis using the same routine laboratory protocol, which remained unchanged throughout the study interval, and were subsequently archived. Only slides with preserved tissue morphology, adequate staining quality, sufficient scan quality, and analyzable tumor-rich regions were retained for quantitative assessment.

The selected IHC markers were interpreted in direct relation to the corresponding morphological pattern and diagnostic tissue compartment. CD20 was used to delineate the CD20-positive B-cell or neoplastic component in most MBCLNs, CD3 was used to estimate the accompanying T-cell infiltrate, and BCL2 was assessed as an anti-apoptotic marker with subtype-dependent diagnostic and biological relevance. For each case, marker distribution was correlated with the tumor-rich region selected on HE review, with

attention to tissue architecture, cellular density, stromal or non-lymphoproliferative components, and the relationship between the neoplastic compartment and the surrounding reactive background.

Whole-slide digitization was performed in the Department of Pathology of the Sibiu Emergency County Clinical Hospital using the Epredia™ 3DHISTECH PANNORAMIC 250 Flash III Digital Scanner in brightfield mode. After scanning, slides were inspected for tissue preservation, staining adequacy, focus quality, and preparation-related or scanning-related artifacts. Slides with technical limitations were additionally reviewed or rescanned using the Pannoramic Desk II Digital Pathology Scanner when this improved digital visualization and region selection. Areas showing major preparation artifacts, staining artifacts, tissue folds, edge artifacts, necrosis, crush artifact, strong background staining, or poor scan focus were avoided during ROI selection.

For each case and each marker-stained slide, one standardized 1 mm^2 ROI was selected after whole-slide review from a viable tumor-rich area with preserved morphology and interpretable IHC staining. ROI selection followed the same sequence for all cases: review of the HE-stained section, identification of the dominant diagnostic tumor compartment, correlation with the available CD20-, CD3-, and BCL2-stained slides, exclusion of necrotic, crushed, folded, poorly focused, or artifact-rich areas, and annotation of a tumor-rich field suitable for exploratory quantitative assessment. For each case, marker-specific ROIs on serial sections were selected to correspond morphologically and overlap as closely as possible. The fixed 1 mm^2 area was used as a common analytical unit across different specimen types and variable archived tissue sizes. The fixed 1 mm^2 area was intended to provide a common analytical area across archived specimens and was not considered a surrogate for the complete spatial heterogeneity of the whole tissue section. Within each slide, limited representative lymphoproliferative/tumor and stromal regions were manually annotated for object-classifier training; the resulting slide-specific classifier was then applied to the whole slide, followed by visual verification and manual correction when required. Within each 1 mm^2 ROI, the lymphoproliferative/tumor compartment and the remaining stromal/non-lymphoproliferative tissue were manually delineated in QuPath with reference to HE morphology and the IHC staining pattern; QuPath area measurements were then used to express each compartment as a percentage of the total ROI area. CD20-positive and CD3-positive cell densities were expressed as positive cells/mm^2, and the CD20/CD3 ratio was calculated as an estimate of the balance between the CD20-positive B-cell or neoplastic compartment and the accompanying CD3-positive T-cell infiltrate.

BCL2 expression was assessed within the annotated lymphoproliferative tumor area, using the HE morphology and the corresponding CD20-stained slide to guide identification of the neoplastic compartment. BCL2-positive tumor cells were evaluated according to both the proportion of stained tumor cells and staining intensity. Intensity was recorded as 1+, 2+, or 3+, and the BCL2 *H*-score was calculated as [1 × (% of 1+ tumor cells) + 2 × (% of 2+ tumor cells) + 3 × (% of 3+ tumor cells)], with a theoretical range from 0 to 300. Intratumoral CD20 density was calculated separately as the number of CD20-positive cells per mm^2 of annotated lymphoproliferative tumor area.

Digital evaluation was coordinated by the author using QuPath v0.6.0 as a research image-analysis platform rather than as a standalone diagnostic tool. Selected image-analysis measurements and technical verification steps were performed with assistance from personnel of the Department of Pathology. The author reviewed the resulting outputs, integrated the final measurements into the study database, and retained responsibility for the analytical decisions and interpretation of the results. For each marker, the digital workflow included whole-slide image import, manual stain-vector calibration, limited training-region annotation, positive-cell detection optimization, slide-specific object-classifier training and application, visual verification, and measurement extraction from the selected 1 mm^2 ROI. Stain-vector calibration, region annotation, positive-cell detection settings, and classifier outputs were checked against the corresponding HE morphology and IHC staining pattern. Detection results were reviewed at the slide level to reduce obvious false-positive and false-negative events caused by background staining, crushed cells, section artifacts, necrosis, stromal structures, overlapping nuclei, poorly segmented nuclei, or non-specific chromogen deposition. The same sequential workflow and visual verification procedure were applied across all included CD20-, CD3-, and BCL2-stained slides, as summarized in Figure 1. The parameter values displayed in Figure 1 represent an illustrative slide-specific configuration. The consistent slide-adaptive workflow used for ROI selection and quantitative IHC assessment is illustrated in Figure 2 (A–D).

Because the archived IHC slides showed between-slide variability in staining intensity, background chromogen deposition, tissue preservation, cellular morphology, and segmentation performance, numerical detection settings were not globally fixed across the cohort. For every CD20-, CD3-, and BCL2-stained slide, stain vectors were manually recalibrated before analysis. The scoring compartment used for 3,3'-Diaminobenzidine (DAB) optical density measurements was selected on a slide-specific basis, using nucleus or cytoplasm as appropriate according to the staining pattern and segmentation performance, and was visually verified before measurement extraction. Detection and segmentation settings, including detection image, background and smoothing parameters, minimum and maximum nuclear area, cell expansion, detection thresholds, scoring compartment, and staining intensity thresholds used for 1+/2+/3+ categorization, were adjusted when required after visual review. A separate object classifier was interactively trained for each slide on limited manually annotated representative lymphoproliferative/tumor and stromal regions and then applied to the whole slide to distinguish these compartments; classifiers were not transferred between slides. No prespecified fixed number of training objects or regions was used; slide-specific training examples were added as required to obtain visually satisfactory compartment separation. After positive-cell detection and object-classifier application, outputs were compared with the corresponding HE morphology and IHC staining pattern. When residual misclassification, overlapping or poorly segmented cells, background signal, or artifact-related errors were identified, the settings were adjusted and the analysis was repeated, manual corrections

were performed, or both approaches were used. Thus, the analytical sequence, one 1 mm^2 ROI per analyzed marker slide, and slide-level visual quality-control procedure were consistent, whereas stain vectors, scoring compartment, object classifiers, and numerical detection settings were slide-specific.

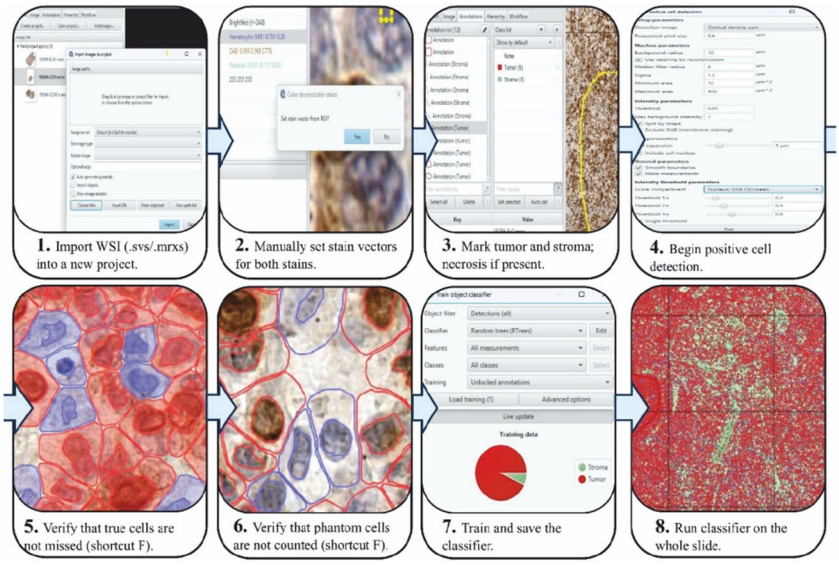

Figure 1 – ***QuPath-based workflow used for digital immunohistochemical quantification. The workflow included WSI import, manual stain-vector calibration, tumor-region annotation, positive-cell detection optimization, slide-specific object-classifier training and application, visual verification, and extraction of measurements from the selected standardized 1 mm^2 region of interest. The parameter values shown in the representative software panels illustrate a slide-specific configuration and were not fixed across the cohort. DAB: 3,3'-Diaminobenzidine; OD: Optical density; WSI: Whole-slide image.***

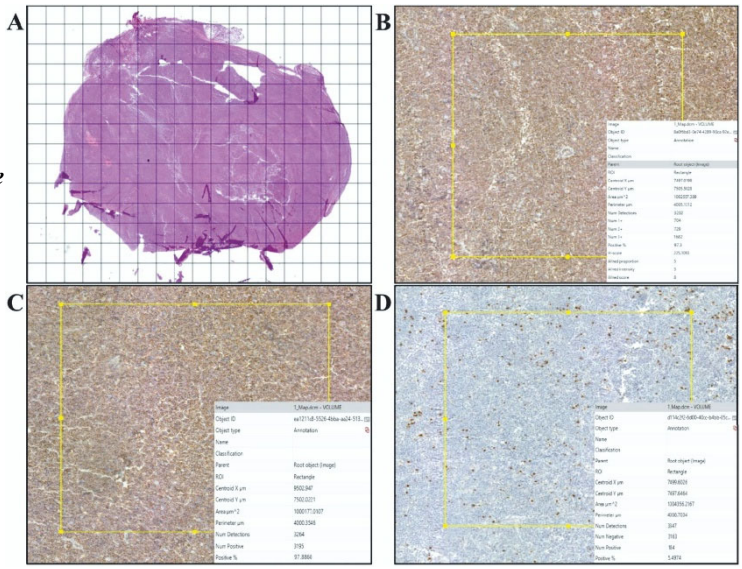

Figure 2 – ***Representative QuPath-assisted digital workflow for standardized ROI selection and quantitative IHC analysis. (A) WSI used for digital analysis. Each grid square corresponds to an area of 1 mm^2, facilitating standardized selection of representative ROIs. (B) Representative ROI selected for BCL2 IHC analysis. (C) Representative ROI selected for CD20 IHC analysis. (D) Representative ROI selected for CD3 IHC analysis. Yellow outlines indicate analyzed regions of approximately 1 mm^2. The displayed QuPath measurements correspond only to the representative fields shown and are included to illustrate the analytical workflow; they do not represent cohort-level averages. BCL2: B-cell lymphoma 2; CD: Cluster of differentiation; IHC: Immunohistochemical; ROI: Region of interest; WSI: Whole-slide image.***

Statistical analysis

Data were entered and organized in Microsoft Excel 2016, while statistical analyses were performed using GraphPad Prism 8.0.1 and IBM Statistical Package for the Social Sciences (SPSS) Statistics 26.0. Categorical variables were summarized as counts and percentages. Continuous variables were summarized using mean ± standard deviation (SD) and/or median with interquartile range, as appropriate. The statistical strategy was structured around descriptive comparison of digitally quantified IHC parameters according to histological subtype and temporal interval, with specimen type retained as an additional contextual variable, and additional subgroup analyses for documented vaccination status and documented prior SARS-CoV-2 infection. Because of the limited sample size, sparse subtype strata, and multiple marker-level comparisons, statistical analyses were interpreted as exploratory.

Fisher's exact test was used for categorical comparisons. For continuous variables, the unpaired Student's *t*-test or Mann–Whitney *U*-test was used for two-group comparisons, while one-way analysis of variance (ANOVA) or Kruskal–Wallis test was used for comparisons involving three or more groups, according to variable distribution and subgroup size. Correlations between quantitative IHC variables were assessed using Spearman's rank correlation coefficient, including CD20-positive cell density, CD3-positive cell density, CD20/CD3 ratio, lymphoproliferative tissue proportion, intratumoral CD20 density, BCL2-positive tumor cell proportion, and BCL2 *H*-score.

Adjusted ordinary least squares regression models with HC3 robust standard errors were constructed for two selected dependent variables: *log*-transformed CD20/CD3 ratio and BCL2 *H*-score. The CD20/CD3 ratio was *log*-transformed because of its right-skewed distribution. Temporal interval, clinical-behavior group, specimen type, age at diagnosis, sex, documented vaccination status, and documented prior COVID-19 history were included as covariates. The pandemic interval, aggressive clinical-behavior group, other specimen

type, female sex, absence of documented vaccination, and absence of documented prior COVID-19 history were used as reference categories. In addition to the main models, a sensitivity analysis excluding mantle cell lymphoma (MCL) cases was performed for BCL2-related temporal comparisons, given the post-restriction clustering of this subtype and its high BCL2 expression profile.

Because the study included multiple subgroups, marker-level, and model-based comparisons, *p*-values were interpreted as nominal. No formal adjustment for multiple testing was applied. A nominal threshold of $p<0.05$ was used to identify statistical signals within the descriptive and exploratory analytical framework.

Results

Cohort selection and baseline characteristics

The initial database query generated 585 lymphoma-related diagnostic records. After general filtering, 366 unique lymphoma-related cases remained for clinical screening, of which 123 fulfilled the study-specific criteria for newly diagnosed MBCLNs. After assessment of tissue availability, IHC-slide availability, scan suitability, and ROI evaluability, 63 cases were retained for digital HP and IHC analysis: 23 diagnosed during the pre-pandemic interval, 19 during the pandemic interval, and 21 during the post-restriction interval. The cohort-selection process is summarized in Figure 3.

Baseline characteristics are summarized in Table 1. The digitally evaluable cohort included 34 (54.0%) men and 29 (46.0%) women, with an overall mean age at diagnosis of 63.6±13.5 years and a median age of 66.0 years. No nominal differences in sex distribution, age at diagnosis, or age-group distribution were detected across temporal intervals. Follow-up duration differed across groups, with shorter follow-up in the post-restriction subgroup.

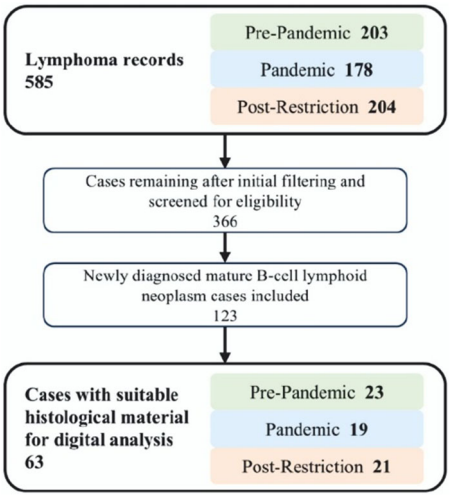

Figure 3 – ***Flowchart of cohort selection from the initially generated lymphoma-related pathology dataset to the final mature B-cell lymphoid neoplasm digital pathology study sample.***

Table 1 – ***Baseline characteristics of the digitally evaluable cohort across temporal subgroups***

Domain	Category	Total *n*=63	Pre-pandemic *n*=23	Pandemic *n*=19	Post-restriction *n*=21	*p*-value
Sex	Male	34 (54.0%)	14 (60.9%)	10 (52.6%)	10 (47.6%)	0.672
	Female	29 (46.0%)	9 (39.1%)	9 (47.4%)	11 (52.4%)	
Age at diagnosis [years]		63.6±13.5 66 (55.5–72.5)	63.5±13.4 67.0 (56.5–71.0)	59.6±14.8 60.0 (53.0–68.0)	67.4±11.7 67.0 (60.0–75.0)	0.192
Age group	<60 years	20 (31.7%)	7 (30.4%)	9 (47.4%)	4 (19.0%)	0.319
	60–74 years	31 (49.2%)	13 (56.5%)	7 (36.8%)	11 (52.4%)	
	≥75 years	12 (19.0%)	3 (13.0%)	3 (15.8%)	6 (28.6%)	
Vaccination	Present	36 (57.1%)	0 (0.0%)	15 (78.9%)	21 (100.0%)	NA
	Absent	27 (42.9%)	23 (100.0%)	4 (21.1%)	0 (0.0%)	
Prior COVID-19 history	Present	5 (7.9%)	0 (0.0%)	4 (21.1%)	1 (4.8%)	NA
	Absent	58 (92.1%)	23 (100.0%)	15 (78.9%)	20 (95.2%)	
Follow-up [months]		29.4±20.1 27.0 (12.0–45.0)	36.9±23.7 30.0 (16.0–61.0)	32.2±18.5 42.0 (13.0–47.0)	18.6±11.4 18.0 (11.0–25.0)	0.018
Final status	Alive under follow-up	50 (79.4%)	19 (82.6%)	15 (78.9%)	16 (76.2%)	0.582
	Lost to follow-up	6 (9.5%)	3 (13.0%)	2 (10.5%)	1 (4.8%)	
	Deceased	7 (11.1%)	1 (4.3%)	2 (10.5%)	4 (19.0%)	

Categorical variables, including sex, age group, documented SARS-CoV-2 vaccination, documented prior SARS-CoV-2 infection, and final status, are presented as *n* (%). Age at diagnosis and follow-up duration are presented as mean ± SD and median (interquartile range). COVID-19: Coronavirus disease 2019; *n*: No. of cases; NA: Not applicable; SARS-CoV-2: Severe acute respiratory syndrome coronavirus 2; SD: Standard deviation.

Subtype and specimen-type distributions are presented in Table 2. The digitally evaluable cohort included the main MBCLN categories encountered in routine diagnostic hematopathology. DLBCL and small lymphocytic lymphoma (SLL) were the most frequent subtypes, with 16 (25.4%) cases each. These were followed by marginal zone lymphoma (MZL) (19.0%), follicular lymphoma (FL), MCL, and hairy cell leukemia (HCL) (7.9% each), lymphoplasmacytic lymphoma (LPL) (4.8%), and plasmablastic lymphoma (PBL) (1.6%). Bone marrow biopsies were the most frequent specimen type (52.4%), followed by lymph node samples (28.6%) and other diagnostic tissue specimens. No nominal global differences in subtype or specimen-type distribution were detected across temporal intervals, although all MCL cases were diagnosed in the post-restriction interval.

Table 2 – ***Distribution of histological subtypes and specimen types in the digitally evaluable cohort across temporal subgroups***

Domain	Category	Total	Pre-pandemic	Pandemic	Post-restriction	*p*-value
Histological subtype	DLBCL	16 (25.4%)	6 (26.1%)	5 (26.3%)	5 (23.8%)	0.259
	SLL	16 (25.4%)	8 (34.8%)	3 (15.8%)	5 (23.8%)	
	MZL	12 (19.0%)	3 (13.0%)	5 (26.3%)	4 (19.0%)	
	FL	5 (7.9%)	2 (8.7%)	2 (10.5%)	1 (4.8%)	
	MCL	5 (7.9%)	0 (0.0%)	0 (0.0%)	5 (23.8%)	
	HCL	5 (7.9%)	2 (8.7%)	3 (15.8%)	0 (0.0%)	
	LPL	3 (4.8%)	1 (4.3%)	1 (5.3%)	1 (4.8%)	
	PBL	1 (1.6%)	1 (4.3%)	0 (0.0%)	0 (0.0%)	
Specimen type	Bone marrow biopsy	33 (52.4%)	11 (47.8%)	13 (68.4%)	9 (42.9%)	0.571
	Lymph node	18 (28.6%)	8 (34.8%)	3 (15.8%)	7 (33.3%)	
	Soft tissue	5 (7.9%)	1 (4.3%)	1 (5.3%)	3 (14.3%)	
	Gastric mucosa	2 (3.2%)	1 (4.3%)	0 (0.0%)	1 (4.8%)	
	Spleen	2 (3.2%)	1 (4.3%)	0 (0.0%)	1 (4.8%)	
	Skin fragment	1 (1.6%)	1 (4.3%)	0 (0.0%)	0 (0.0%)	
	Pericardium	1 (1.6%)	0 (0.0%)	1 (5.3%)	0 (0.0%)	
	Ileal mucosa	1 (1.6%)	0 (0.0%)	1 (5.3%)	0 (0.0%)	

Histological subtypes and specimen types are presented as *n* (%). *p*-values were interpreted as nominal exploratory values. DLBCL: Diffuse large B-cell lymphoma; FL: Follicular lymphoma; HCL: Hairy cell leukemia; LPL: Lymphoplasmacytic lymphoma; MCL: Mantle cell lymphoma; MZL: Marginal zone lymphoma; *n*: No. of cases; PBL: Plasmablastic lymphoma; SLL: Small lymphocytic lymphoma.

Immunohistochemical variation according to histological subtype

The quantitative IHC profile according to histological subtype is summarized in Table 3.

Subtype-stratified analysis showed the largest differences in the digitally quantified IHC profile. CD20- and CD3-positive cell density, CD20/CD3 ratio (Figure 4A), BCL2-positive tumor cell proportion, and BCL2 *H*-score (Figure 4B) varied across histological subtypes. BCL2-related parameters were especially sensitive to subtype composition, with the highest mean values observed in MCL. PBL, represented by a single case, showed low CD20-positive and BCL2-related values. DLBCL, SLL, FL, MZL, HCL, and LPL showed distinct combinations of CD20-positive cell density, CD3-positive infiltration, CD20/CD3 balance, and BCL2 expression, reflecting the entity-level heterogeneity of the cohort. The subtype-related distributions selected for visual emphasis are shown in Figure 4 (C and D).

To complement the quantitative analyses, representative HP and IHC findings from selected cases included in the digitally evaluable cohort are presented in Figure 5 (A–L). These representative fields illustrate the morphological appearance of HCL and DLBCL together with the corresponding BCL2, CD20, and CD3 immunostaining, highlighting the relationship between tumor morphology, the neoplastic B-cell population, and the accompanying reactive T-cell infiltrate.

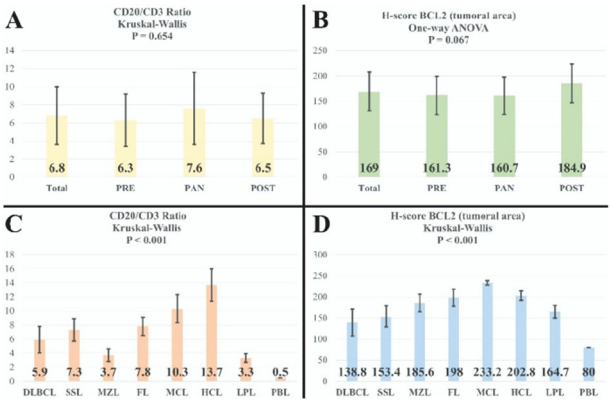

Figure 4 – ***Composite graphical summary of the principal comparisons in the study. ANOVA: Analysis of variance; BCL2: B-cell lymphoma 2; CD: Cluster of differentiation; DLBCL: Diffuse large B-cell lymphoma; FL: Follicular lymphoma; HCL: Hairy cell leukemia; LPL: Lymphoplasmacytic lymphoma; MCL: Mantle cell lymphoma; MZL: Marginal zone lymphoma; PAN: Pandemic; PBL: Plasmablastic lymphoma; PRE: Pre-pandemic; POST: Post-restriction; SLL: Small lymphocytic lymphoma.***

Table 3 – ***Digital immunohistochemical parameters according to histological subtype***

Variable	DLBCL	SLL	MZL	FL	MCL	HCL	LPL	PBL*	*p*-value
CD20-positive cells/mm²	1930.2±751.8 1921.5 (1247.5–2599.2)	1546.9±527.0 1584.5 (1152.8–1819.0)	2470.2±677.7 2504.5 (2039.8–2754.2)	3417.8±1219.0 3486 (3193.0–4250.0)	4265.6±1666.4 3452 (3100.0–4790.0)	2486.4±500.7 2313 (2300.0–2840.0)	1548.3±542.0 1823 (1373.5–1860.5)	286.0±0.0 286 (286.0–286.0)	<0.001
CD3-positive cells/mm²	339.4±138.7 350.5 (223.2–434.2)	223.9±100.8 222 (131.2–277.8)	735.1±350.8 637 (470.2–1019.8)	451.0±183.3 519 (369.0–552.0)	411.2±105.9 423 (356.0–476.0)	182.8±32.9 186 (163.0–194.0)	458.3±135.4 476 (395.5–530.0)	609.0±0.0 609 (609.0–609.0)	<0.001
CD20/CD3 ratio	5.9±1.9 5.7 (4.5–6.7)	7.3±1.6 7 (6.5–8.5)	3.7±0.9 4 (3.1–4.4)	7.8±1.3 8.6 (6.6–8.7)	10.3±2.0 10.1 (8.7–11.5)	13.7±2.3 12.4 (12.4–16.1)	3.3±0.6 3.1 (3.0–3.6)	0.5±0.0 0.5 (0.5–0.5)	<0.001

Variable	DLBCL	SLL	MZL	FL	MCL	HCL	LPL	PBL*	*p*-value
BCL2-positive tumor cells [%]	69.9±11.1 71.0 (62.2–77.5)	73.4±9.8 71.5 (67.0–79.8)	83.6±6.7 80.5 (78.0–89.0)	88.8±5.8 90.0 (85.0–93.0)	97.0±2.5 98.0 (96.0–99.0)	90.8±2.3 90.0 (90.0–92.0)	78.0±3.6 77.0 (76.0–79.5)	49.0±0.0 49.0 (49.0–49.0)	<0.001
BCL2 H-score	138.8±31.8 141.0 (106.2–164.5)	153.4±24.9 150.0 (138.2–164.8)	185.6±20.6 182.0 (168.8–206.8)	198.0±20.3 197.0 (180.0–204.0)	233.2±5.2 231.0 (229.0–236.0)	202.8±10.9 197.0 (195.0–212.0)	164.7±15.0 164.0 (157.0–172.0)	80.0±0.0 80.0 (80.0–80.0)	<0.001

Values are presented as mean ± SD and median (interquartile range). Subtype-level comparisons were interpreted descriptively because several subtype groups were small. *p*-values were interpreted as nominal exploratory values. *Values reported for PBL should be interpreted descriptively only, because this subtype was represented by a single case. BCL2: B-cell lymphoma 2; CD: Cluster of differentiation; DLBCL: Diffuse large B-cell lymphoma; FL: Follicular lymphoma; HCL: Hairy cell leukemia; LPL: Lymphoplasmacytic lymphoma; MCL: Mantle cell lymphoma; MZL: Marginal zone lymphoma; PBL: Plasmablastic lymphoma; SD: Standard deviation; SLL: Small lymphocytic lymphoma.

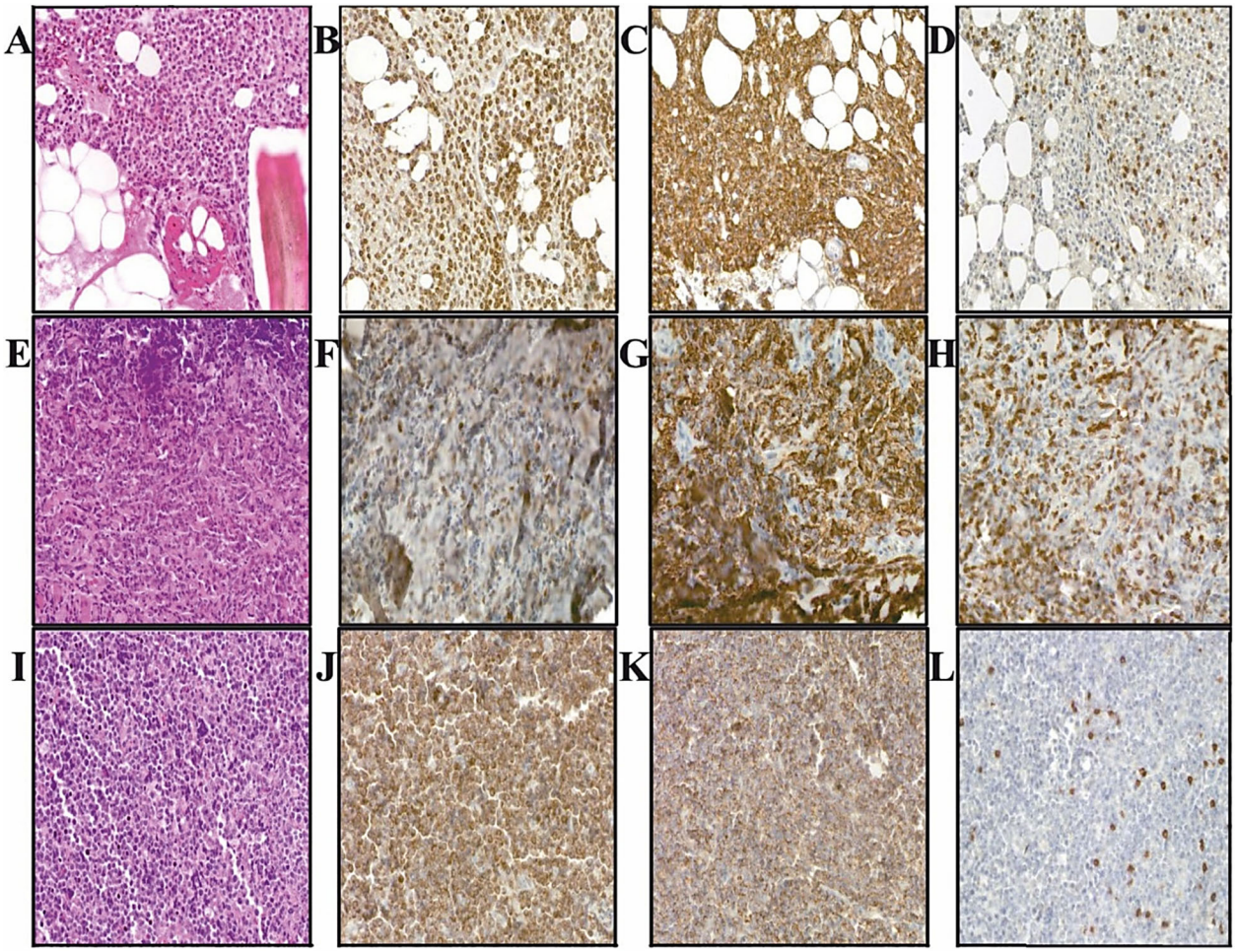

Figure 5 – ***Representative histopathological and immunohistochemical findings in HCL and DLBCL. (A–D) HCL involving the bone marrow. HE staining demonstrates diffuse marrow infiltration by small atypical lymphoid cells with abundant pale cytoplasm and reduced residual hematopoiesis (A). BCL2 immunostaining shows diffuse expression within the neoplastic infiltrate (B). CD20 highlights the neoplastic B-cell population (C), whereas CD3 identifies the accompanying reactive T-cell component (D). (E–H) DLBCL diagnosed in a biopsy from the thyroid region. HE staining demonstrates diffuse infiltration of soft tissue by large atypical lymphoid cells with irregular nuclear contours and conspicuous nucleoli (E). BCL2 is expressed in the neoplastic cells (F). CD20 highlights the diffuse large B-cell population (G), while CD3 demonstrates the admixed reactive T-cell infiltrate (H). (I–L) DLBCL involving the abdominal wall. HE staining shows a diffuse proliferation of medium-to-large atypical lymphoid cells (I). BCL2 expression is present in the neoplastic population (J). CD20 highlights the neoplastic B-cells (K), whereas CD3 demonstrates the accompanying reactive T-cell infiltrate (L). Representative fields were selected from whole-slide images viewed in QuPath at ×40 objective magnification. BCL2: B-cell lymphoma 2; CD: Cluster of differentiation; DLBCL: Diffuse large B-cell lymphoma; HCL: Hairy cell leukemia; HE: Hematoxylin–Eosin.***

Temporal comparison of immunohistochemical parameters

The quantitative IHC profile across temporal subgroups is summarized in Table 4.

Mean CD20-positive and CD3-positive cell densities in the overall cohort were 2239.0±1130.2 cells/mm^2 and 397.5±260.9 cells/mm^2, respectively. Both variables showed numerically higher mean values in the post-restriction interval, without reaching the nominal $p<0.05$ threshold. The CD20/CD3 ratio showed a similar distribution across the three intervals, with median values ranging from 6.3 to 6.8.

Table 4 – ***Digital immunohistochemical parameters across temporal subgroups***

Variable	Total	Pre-pandemic	Pandemic	Post-restriction	*p*-value
CD20-positive cells/mm²	2239.0±1130.2 2060 (1521.5–2801.5)	2027.8±1027.4 1852 (1502.0–2573.5)	1941.1±737.1 2013 (1329.0–2358.5)	2739.8±1382.4 2639 (1763.0–3100.0)	0.09
CD3-positive cells/mm²	397.5±260.9 354 (214.5–501.0)	392.1±266.1 347.0 (222.0–497.5)	311.4±179.8 272 (180.0–413.5)	481.3±299.3 423 (264.0–584.0)	0.092
CD20/CD3 ratio	6.8±3.2 6.6 (4.4–8.7)	6.3±2.9 6.3 (4.2–8.1)	7.6±4.0 6.8 (4.6–9.3)	6.5±2.8 6.6 (4.5–8.2)	0.654
Lymphoproliferative component [%]	64.9±16.4 63 (53.5–77.0)	65.4±17.8 65 (51.0–78.0)	59.6±13.7 62 (45.5–68.0)	69.1±16.3 63 (59.0–84.0)	0.184
Other tissues [%]	35.1±16.4 37 (23.0–46.5)	34.6±17.8 35 (22.0–49.0)	40.4±13.7 38 (32.0–54.5)	30.9±16.3 37 (16.0-41.0)	0.184
Intratumoral CD20 density (per mm² tumor area)	3403.0±1267.6 3179.5 (2492.9–4259.1)	3099.5±1248.7 3038.3 (2424.0–3581.7)	3216.4±885.7 3418.2 (2584.6–3774.0)	3904.2±1468.8 3314.5 (2754.7–5059.5)	0.226
BCL2-positive tumor cells [%]	78.8±12.5 79 (70.5–89.0)	74.8±11.9 76 (68.0–82.0)	77.4±12.7 78 (68.5–88.0)	84.3±11.6 86 (79.0–93.0)	0.033
BCL2 H-score (tumor area)	169.0±38.5 170.0 (144.0–196.5)	161.3±37.0 163.0 (141.5–183.0)	160.7±37.2 162.0 (129.0–186.5)	184.9±38.2 191 (164.0–209.0)	0.067

Continuous variables are presented as mean ± SD and median (interquartile range). *p*-values were interpreted as nominal exploratory values. BCL2: B-cell lymphoma 2; CD: Cluster of differentiation; SD: Standard deviation.

The percentage of lymphoproliferative tissue, the proportion of other tissue components, and intratumoral CD20 density showed no nominal temporal differences. The post-restriction subgroup showed numerically higher mean whole-area CD20-positive cell density and intratumoral CD20 density than the pre-pandemic and pandemic subgroups.

In the overall cohort, BCL2-related variables showed an apparent interval-related pattern. BCL2-positive tumor cell proportion increased from 74.8±11.9% in the pre-pandemic interval to 84.3±11.6% in the post-restriction interval, with a nominal global difference. The BCL2 *H*-score followed a similar direction, increasing from 161.3±37.0 in the pre-pandemic interval and 160.7±37.2 in the pandemic interval to 184.9±38.2 in the post-restriction interval. Given the uneven subtype composition across intervals, this overall-cohort pattern was interpreted cautiously and was reassessed in sensitivity analyses excluding MCL. Selected temporal distributions are shown in Figure 4A.

Contextual variables, correlations, and adjusted models

Within the pandemic and post-restriction subset, documented vaccination status was evaluated as a contextual variable in relation to the main digital IHC parameters. No nominal differences were detected in this small, highly imbalanced exploratory comparison (36 vaccinated *vs.* 4 unvaccinated cases) for the CD20-, CD3-, and BCL2-related parameters presented in Table 5.

Pandemic and post-restriction cases were also grouped according to documented SARS-CoV-2 infection before lymphoma diagnosis and tissue sampling. Most digitally quantified IHC variables showed no nominal differences according to documented prior infection status. The CD20/CD3 ratio was numerically higher in the five cases with documented prior infection than in those without such documentation (10.4±3.4 *vs.* 6.6±3.2; p=0.016); given the very small subgroup, this nominal signal was treated as a hypothesis-generating exploratory observation rather than evidence of a biological association. The remaining CD20-, CD3-, and BCL2-related parameters showed no nominal differences (Table 6).

Table 5 – ***Comparative analysis according to documented SARS-CoV-2 vaccination status in pandemic and post-restriction cases***

Variable	Unvaccinated (PAN+POST)	Vaccinated (PAN+POST)	*p*-value
Age at diagnosis [years]	65.8±14.5	63.5±13.7	0.756
Clinical-behavior group – aggressive	3 (75.0%)	20 (55.6%)	0.624
Clinical-behavior group – indolent	1 (25.0%)	16 (44.4%)	
CD20-positive cells/mm²	1688.0±550.4	2435.1±1212.4	0.207
CD3-positive cells/mm²	324.8±175.6	409.0±269.6	0.712
CD20/CD3 ratio	6.1±2.3	7.2±3.5	0.778
Intratumoral CD20 density (per mm² tumor area)	2751.4±672.4	3669.3±1282.8	0.170
BCL2-positive tumor cells [%]	75.2±8.5	81.7±12.8	0.259
BCL2 3+ tumor cells [%]	17.5±7.4	28.4±13.6	0.124
BCL2 H-score (tumor area)	146.5±25.6	176.4±39.5	0.151

Categorical variables are presented as *n* (%). Continuous variables are presented as mean ± SD. This analysis was restricted to cases diagnosed during the pandemic and post-restriction intervals. Data were interpreted descriptively because documented vaccination status was closely related to calendar period and the number of unvaccinated cases was small. No nominal differences were detected in this highly imbalanced comparison; this should be interpreted as absence of evidence rather than evidence of absence. *p*-values were interpreted as nominal exploratory values. BCL2: B-cell lymphoma 2; CD: Cluster of differentiation; *n*: No. of cases; PAN+POST: Combined pandemic and post-restriction intervals; SARS-CoV-2: Severe acute respiratory syndrome coronavirus 2; SD: Standard deviation.

Table 6 – ***Comparative analysis according to documented prior SARS-CoV-2 infection history in pandemic and post-restriction cases***

Variable	No prior COVID-19 history (PAN+POST)	Prior COVID-19 history (PAN+POST)	*p*-value
Age at diagnosis [years]	63.3±14.1	66.4±10.3	0.642
Clinical behavior group – aggressive	20 (57.1%)	3 (60.0%)	1.000
Clinical behavior group – indolent	15 (42.9%)	2 (40.0%)	
CD20-positive cells/mm²	2314.1±1173.3	2684.2±1319.1	0.551
CD3-positive cells/mm²	420.1±270.8	263.8±124.2	0.197
CD20/CD3 ratio	6.6±3.2	10.4±3.4	0.016

Variable	No prior COVID-19 history (PAN+POST)	Prior COVID-19 history (PAN+POST)	*p*-value
Intratumoral CD20 density (per mm² tumor area)	3574.7±1291.5	3597.0±1148.0	0.775
BCL2-positive tumor cells [%]	80.2±12.7	87.2±9.4	0.243
BCL2 3+ tumor cells [%]	27.0±13.5	30.0±14.7	0.644
BCL2 H-score (tumor area)	171.6±40.1	185.8±32.7	0.456
Follow-up [months]	24.6±15.8	28.4±22.4	0.697

Categorical variables are presented as *n* (%). Continuous variables are presented as mean ± SD. *p*-values were interpreted as nominal exploratory values. Because only five cases had documented prior SARS-CoV-2 infection, the CD20/CD3 ratio comparison should be regarded as a hypothesis-generating nominal signal rather than evidence of a biological association. BCL2: B-cell lymphoma 2; CD: Cluster of differentiation; COVID-19: Coronavirus disease 2019; *n*: No. of cases; PAN+POST: Combined pandemic and post-restriction intervals; SARS-CoV-2: Severe acute respiratory syndrome coronavirus 2; SD: Standard deviation.

The complete correlation matrix is summarized in Table 7. CD20-positive cell density correlated positively with CD3-positive cell density, lymphoproliferative tissue percentage, intratumoral CD20 density, BCL2-positive tumor cell proportion, and BCL2 *H*-score. CD3-positive cell density correlated negatively with the CD20/CD3 ratio. Among the BCL2-related measurements, BCL2-positive tumor cell proportion and BCL2 *H*-score showed the strongest positive correlation. The observed correlation pattern linked whole-area CD20-positive cell density with both the annotated lymphoproliferative compartment and BCL2-related tumor cell measurements.

The adjusted models are summarized in Table 8. In the model for *log*-transformed CD20/CD3 ratio, lymph node samples and bone marrow samples showed higher adjusted values than other specimen types. The coefficient for documented prior COVID-19 history was positive for *log*-transformed CD20/CD3 ratio, but the confidence interval narrowly crossed zero; given the five cases with documented prior infection, this estimate was interpreted as unstable and exploratory.

Table 7 – ***Correlation matrix of quantitative digital immunohistochemical variables***

Variable	CD20-positive cells/mm²	CD3-positive cells/mm²	CD20/CD3 ratio	Lymphoproliferative tissue [%]	Intratumoral CD20 density (per mm² tumor area)	BCL2-positive tumor cells [%]	BCL2 *H*-score (tumor area)
CD20-positive cells/mm²	–	*ρ*=0.611 *p*<0.001	*ρ*=0.195 *p*=0.127	*ρ*=0.598 *p*<0.001	*ρ*=0.829 *p*<0.001	*ρ*=0.520 *p*<0.001	*ρ*=0.543 *p*<0.001
CD3-positive cells/mm²	*ρ*=0.611 *p*<0.001	–	*ρ*=-0.598 *p*<0.001	*ρ*=0.380 *p*=0.002	*ρ*=0.555 *p*<0.001	*ρ*=0.190 *p*=0.135	*ρ*=0.224 *p*=0.077
CD20/CD3 ratio	*ρ*=0.195 *p*=0.127	*ρ*=-0.598 *p*<0.001	–	*ρ*=0.213 *p*=0.094	*ρ*=0.098 *p*=0.443	*ρ*=0.281 *p*=0.026	*ρ*=0.260 *p*=0.040
Lymphoproliferative tissue [%]	*ρ*=0.598 *p*<0.001	*ρ*=0.380 *p*=0.002	*ρ*=0.213 *p*=0.094	–	*ρ*=0.115 *p*=0.370	*ρ*=-0.002 *p*=0.986	*ρ*=0.005 *p*=0.971
Intratumoral CD20 density (per mm² tumor area)	*ρ*=0.829 *p*<0.001	*ρ*=0.555 *p*<0.001	*ρ*=0.098 *p*=0.443	*ρ*=0.115 *p*=0.370	–	*ρ*=0.687 *p*<0.001	*ρ*=0.720 *p*<0.001
BCL2-positive tumor cells [%]	*ρ*=0.520 *p*<0.001	*ρ*=0.190 *p*=0.135	*ρ*=0.281 *p*=0.026	*ρ*=-0.002 *p*=0.986	*ρ*=0.687 *p*<0.001	–	*ρ*=0.941 *p*<0.001
BCL2 H-score (tumor area)	*ρ*=0.543 *p*<0.001	*ρ*=0.224 *p*=0.077	*ρ*=0.260 *p*=0.040	*ρ*=0.005 *p*=0.971	*ρ*=0.720 *p*<0.001	*ρ*=0.941 *p*<0.001	–

Correlations were assessed using Spearman's rank correlation coefficient. Values are presented as *rho* coefficients, with *p*-values shown where applicable. *p*-values were interpreted as nominal exploratory values. BCL2: B-cell lymphoma 2; CD: Cluster of differentiation.

Table 8 – ***Exploratory adjusted regression models for log-transformed CD20/CD3 ratio and BCL2 H-score***

Outcome	Covariate	Beta coefficient	95% CI	*p*-value
Log-transformed CD20/CD3 ratio	Post-restriction period	-0.146	-0.579 to 0.287	0.510
	Pre-pandemic period	-0.117	-0.610 to 0.376	0.642
	Indolent clinical behavior group	-0.203	-0.51 to 0.111	0.206
	Lymph node specimen group	0.5	0.168 to 0.832	0.003
	Bone marrow specimen group	0.339	0.007 to 0.670	0.045
	Age at diagnosis	0.001	-0.012 to 0.014	0.878
	Sex M	-0.132	-0.391 to 0.127	0.319
	Vaccinated	0.094	-0.377 to 0.565	0.697
	Prior COVID-19 history	0.471	-0.003 to 0.946	0.051
BCL2 H-score	Post-restriction period	39.152	17.513 to 60.790	<0.001
	Pre-pandemic period	20.653	0.968 to 40.337	0.04
	Indolent clinical behavior group	42.08	27.947 to 56.214	<0.001
	Lymph node specimen group	-7.095	-29.115 to 14.925	0.528
	Bone marrow specimen group	-0.689	-17.960 to 16.583	0.938
	Age at diagnosis	0.546	-0.087 to 1.178	0.091
	Sex M	6.46	-8.824 to 21.744	0.407
	Vaccinated	2.57	-19.354 to 24.493	0.818
	Prior COVID-19 history	12.244	-16.942 to 41.430	0.411

Models were fitted using ordinary least squares regression with HC3 robust standard errors. The pandemic interval, aggressive clinical behavior group, other specimen type, female sex, absence of documented vaccination, and absence of documented prior COVID-19 history were used as reference categories. *p*-values were interpreted as nominal exploratory values. BCL2: B-cell lymphoma 2; CD: Cluster of differentiation; CI: Confidence interval; COVID-19: Coronavirus disease 2019; M: Male.

In the model for BCL2 *H*-score, both the post-restriction interval and the pre-pandemic interval showed higher adjusted values than the pandemic reference interval, with the larger adjusted difference observed for the post-restriction interval. The indolent clinical-behavior group also showed higher adjusted BCL2 *H*-score values than the aggressive clinical-behavior group. Specimen type, age at diagnosis, sex, documented vaccination status, and documented prior COVID-19 history showed no nominal adjusted association with BCL2 *H*-score.

Sensitivity analyses focused on BCL2-related temporal patterns

Additional analyses were performed to evaluate the BCL2-related temporal pattern observed in the whole cohort. These analyses included exclusion of MCL cases, subtype-restricted comparisons in DLBCL and SLL, and phenotype-restricted subgroup combinations based on relatively comparable BCL2-related expression profiles. The temporal sensitivity analyses are summarized in Table 9.

Table 9 – ***Sensitivity analyses for digitally quantified immunohistochemical parameters across temporal intervals***

Analysis	Variable	Pre-pandemic *n*; mean ± SD	Pandemic *n*; mean ± SD	Post-restriction *n*; mean ± SD	*p*-value
Excluding MCL	BCL2-positive tumor cells [%]	23; 74.8±11.9	19; 77.4±12.7	16; 80.4±10.3	0.335
	BCL2 *H*-score (tumor area)	23; 161.3±37.0	19; 160.7±37.2	16; 169.8±30.2	0.699
	BCL2 3+ tumor cells [%]	23; 26.1±10.2	19; 22.6±11.0	16; 24.9±8.4	0.424
DLBCL	BCL2-positive tumor cells [%]	6; 67.8±8.6	5; 63.8±9.4	5; 78.6±11.6	0.090
	BCL2 *H*-score (tumor area)	6; 134.8±21.2	5; 120.8±25.5	5; 161.6±38.8	0.119
	CD20-positive cells/mm^2	6; 1944.3±738.1	5; 1688.4±695.0	5; 2155.0±904.8	0.529
	CD3-positive cells/mm^2	6; 356.5±116.8	5; 284.4±142.8	5; 373.8±170.2	0.481
	CD20/CD3 ratio	6; 5.6±2.2	5; 6.4±2.2	5; 5.9±1.2	0.554
SLL	BCL2-positive tumor cells [%]	8; 72.4±8.6	3; 71.7±12.9	5; 76.0±11.6	0.790
	BCL2 *H*-score (tumor area)	8; 158.5±28.3	3; 136.7±14.4	5; 155.2±23.4	0.394
	CD20-positive cells/mm^2	8; 1527.5±632.6	3; 1360.7±569.2	5; 1689.8±356.2	0.599
	CD3-positive cells/mm^2	8; 220.0±110.3	3; 161.3±96.0	5; 267.6±82.9	0.247
	CD20/CD3 ratio	8; 7.2±1.3	3; 9.0±1.8	5; 6.6±1.5	0.134
DLBCL + SLL	BCL2-positive tumor cells [%]	14; 70.4±8.6	8; 66.8±10.7	10; 77.3±11.0	0.098
	BCL2 *H*-score (tumor area)	14; 148.4±27.4	8; 126.8±22.3	10; 158.4±30.4	0.053
DLBCL + SLL + LPL	BCL2-positive tumor cells [%]	15; 71.2±8.8	9; 67.9±10.6	11; 77.1±10.5	0.128
	BCL2 *H*-score (tumor area)	15; 150.5±27.6	9; 129.3±22.3	11; 158.9±28.9	0.048
MZL + FL + HCL	BCL2-positive tumor cells [%]	7; 86.1±6.9	10; 86.0±7.0	5; 87.6±5.6	0.939
	BCL2 *H*-score (tumor area)	7; 196.3±20.3	10; 188.9±21.3	5; 193.6±17.5	0.768

Values are expressed as *n*; mean ± SD. The *p*-value corresponds to the Kruskal–Wallis test for comparison across the three temporal intervals. BCL2: B-cell lymphoma 2; CD: Cluster of differentiation; DLBCL: Diffuse large B-cell lymphoma; FL: Follicular lymphoma; HCL: Hairy cell leukemia; LPL: Lymphoplasmacytic lymphoma; MCL: Mantle cell lymphoma; MZL: Marginal zone lymphoma; *n*: No. of cases; SD: Standard deviation; SLL: Small lymphocytic lymphoma.

After exclusion of MCL cases, the temporal difference in BCL2-positive tumor cell proportion was no longer nominally significant, with mean values of 74.8±11.9% in the pre-pandemic interval, 77.4±12.7% in the pandemic interval, and 80.4±10.3% in the post-restriction interval. A similar pattern was observed for BCL2 *H*-score, with mean values of 161.3±37.0, 160.7±37.2, and 169.8±30.2, respectively. BCL2 3+ tumor cell proportion also showed no nominal temporal differences after exclusion of MCL cases.

In the DLBCL-restricted analysis, BCL2-positive tumor cell proportion and BCL2 *H*-score were numerically higher in the post-restriction subgroup, but the temporal comparisons did not reach the nominal $p<0.05$ threshold. In the SLL-restricted analysis, BCL2-related parameters and CD20/CD3 balance showed no nominal temporal differences. In the combined DLBCL and SLL subset, selected because these were the two largest subtype groups with relatively overlapping BCL2-related descriptive values, BCL2-positive tumor cell proportion and BCL2 *H*-score also showed numerically higher post-restriction values, with *p*-values remaining above the nominal significance threshold.

Additional phenotype-restricted combinations were also evaluated. In the DLBCL + SLL + LPL subset, BCL2-positive tumor cell proportion showed no nominal temporal difference, while BCL2 *H*-score showed a nominal difference, with lower values in the pandemic interval and higher values in the post-restriction interval. In the MZL + FL + HCL subset, BCL2-positive tumor cell proportion and BCL2 *H*-score showed no nominal temporal differences.

Discussions

In this single-center digital HP and IHC study, histological subtype was the main source of variation in quantified CD20-, CD3-, and BCL2-related parameters, consistent with lymphoma classification and tumor microenvironment literature [1–5].

Subtype-related BCL2 heterogeneity was central to the temporal interpretation. MCL, FL, and HCL showed high BCL2-related values, whereas the single PBL case showed low CD20 and BCL2 values, illustrating the marked entity-level heterogeneity of the cohort. In DLBCL, BCL2 expression has established biological and prognostic relevance, and IHC assessment has been evaluated as a clinically informative biomarker [13, 14]. Because all MCL cases occurred in the post-restriction interval and MCL had the highest BCL2 *H*-score, MCL exclusion substantially attenuated the temporal pattern; DLBCL- and SLL-restricted analyses likewise showed no nominal temporal differences.

Temporal stratification remained a secondary contextual analysis. Most CD20- and CD3-related variables showed no nominal interval differences. The clinical importance of COVID-19 in patients with hematological malignancies has been well documented [23]. Changes in diagnostic access, cancer detection, referral pathways, and case ascertainment during the pandemic have been described in lymphoma and broader cancer-care studies [17, 24–26], providing a plausible contextual explanation for differences in the composition of cases reaching tissue diagnosis. Although temporal interval remained associated with BCL2 *H*-score in the exploratory adjusted model, the binary clinical-behavior grouping could not fully capture entity-level heterogeneity; the marked attenuation after MCL exclusion therefore supports a substantial case-mix contribution.

The CD20/CD3 measurements were intended as descriptive tissue-level measures of the B-cell or neoplastic and accompanying T-cell compartments, not as a validated biological or prognostic index. This approach is consistent with studies showing that immune and stromal composition can define biologically meaningful features of large B-cell lymphoma [27, 28].

Digital image-analysis and spatial pathology studies have linked T-cell infiltration, immunoscore-type measurements, recurrent cellular neighborhoods, immune-escape patterns, and spatially organized tumor-immune interactions with biologically or clinically relevant features in DLBCL [12, 29–36]. The present study did not attempt to reproduce those spatial or prognostic models; CD3 patterns were interpreted morphologically with HE review and marker-level verification.

Prior SARS-CoV-2 infection and vaccination were contextual variables. COVID-related T-cell lymphopenia and apoptosis-related immune dysfunction [37, 38], as well as vaccination-associated germinal-center responses and lymphadenopathy [39–41], provide biological context but were not directly assessed here. The higher CD20/CD3 ratio in five cases with documented prior infection was therefore interpreted exploratorily because of sparse exposure and incomplete infection data. Likewise, no nominal IHC differences were detected in the imbalanced vaccination comparison (36 vaccinated *vs.* 4 unvaccinated), which does not establish absence of an effect. A lymphoma-specific study did not support vaccination as a trigger for ipsilateral malignant B-cell non-Hodgkin lymphoma [42].

QuPath provides an open-source platform for quantitative digital pathology [7], and previous lymphoma-related studies have demonstrated QuPath-assisted or artificial intelligence (AI)-assisted IHC assessment [8, 9, 12]. Quantitative image analysis has also been used to refine tumor-specific BCL2 assessment in DLBCL [43]. In the present study, QuPath-assisted analysis enabled quantitative extraction from archived lymphoma slides using whole-slide review, tumor-rich region selection, stain-vector calibration, positive-cell detection, slide-specific classifier application, and visual verification; the workflow remained morphology-guided rather than a standalone diagnostic method.

Limitations

Several limitations should be considered. First, this single-center retrospective study included 63 digitally evaluable cases, producing small strata after subdivision by histological subtype and contextual variables; PBL was represented by one case. Inclusion also depended on archived tissue and slide availability, staining and scan quality, and ROI evaluability, potentially selecting a technically favorable subset.

Second, subtype composition affected the temporal analyses. All MCL cases occurred in the post-restriction interval and had the highest BCL2-related values; MCL exclusion attenuated the apparent temporal BCL2 pattern. Individual-subtype adjustment was not reliable because of sparse strata, while the binary clinical-behavior grouping did not fully capture entity-level histological heterogeneity. The adjusted models also carried substantial overfitting risk given the sample size and number of covariates, so coefficients and confidence intervals should be interpreted as exploratory estimates.

Third, vaccination and prior COVID-19 history were available only as binary variables. Important exposure details were unavailable, undocumented prior infection could not be excluded, and only five cases had documented prior infection. Vaccination was closely related to calendar period and highly imbalanced (36 vaccinated *vs.* 4 unvaccinated), limiting both subgroup and adjusted interpretations.

Fourth, digital measurements remained sensitive to slide quality, staining intensity, artifacts, region selection, classifier performance, and visual verification. One 1 mm^2 tumor-rich ROI per marker slide did not capture the full spatial heterogeneity of the tissue, and exact spatial co-registration across serial marker sections was not always possible. Region selection, classifier training, parameter optimization, and final verification were performed within a morphology-guided, partly operator-dependent workflow, with selected technical assistance from personnel of the Department of Pathology. The analysis was not formally blinded to histological subtypes or to the clinical and temporal contextual variables. No formal intraobserver or interobserver reproducibility study, independent validation set, or classifier-performance assessment against a manually annotated reference standard was performed. In addition, the number of training objects and the extent of manual corrections were not systematically recorded at object level. Because stain vectors, classifiers, detection parameters, scoring compartments, and intensity thresholds were optimized at slide level, exact parameter-level reproducibility and absolute between-slide comparability were limited, particularly for intensity-derived BCL2 measurements and *H*-score. Accordingly, the QuPath-derived measurements should be interpreted as exploratory, morphology-guided research measurements rather than as outputs of a formally validated digital assay with established analytical comparability across slides. Preanalytical and staining-batch variation among archived slides also cannot be excluded, despite use of the same routine staining protocol throughout the study interval.

Fifth, the dataset lacked structured variables for disease stage, lactate dehydrogenase, Ki67, treatment, response, survival modeling, and molecular profiling. The study therefore remained focused on tissue morphology, routine immunohistochemistry, and digital quantification rather than prognostic or therapeutic associations.

Conclusions

In this single-center study of MBCLNs, histological subtype was the main determinant of the digitally quantified

CD20-, CD3-, and BCL2-related profile, emphasizing interpretation of quantitative IHC data within entity-level morphology and immunophenotype.

Temporal stratification provided secondary contextual information. Most CD20- and CD3-related variables showed no nominal interval differences, whereas the apparent BCL2 pattern was substantially attenuated after MCL exclusion. Together with the subtype-restricted analyses, this indicates that case mix contributed importantly to the temporal BCL2 signal, while the residual adjusted-model association cannot be separated confidently from incompletely captured subtype heterogeneity. Vaccination comparisons were highly imbalanced, and the higher CD20/CD3 ratio in five cases with documented prior COVID-19 history remains hypothesis-generating.

QuPath-assisted analysis provided quantitative tissue-level measurements through a morphology-guided, slide-adaptive workflow with visual verification. This approach can support retrospective assessment of archived lymphoma material while remaining integrated with conventional HP interpretation and the biological heterogeneity of individual lymphoma entities.

Author's contributions

P.-C.T. was responsible for study conception and design, case selection, data curation, statistical analysis, interpretation of the results, manuscript drafting, critical revision of the manuscript, and approval of the final version. The author coordinated the digital image-analysis workflow, integrated the resulting measurements into the study database, interpreted the quantitative findings, and remained responsible for the final content of the manuscript.

Conflict of interests

The author declares that there is no conflict of interests.

Funding

This research received no external funding.

Acknowledgments

This manuscript was developed within the author's broader doctoral research framework on malignant hematological diseases during the COVID-19 pandemic. The author thanks A.V. and I.G. for assistance with selected QuPath measurements and technical verification of image-analysis outputs. The author also acknowledges the pathologists of the Department of Pathology of the Sibiu Emergency County Clinical Hospital, Sibiu, Romania, whose routine diagnostic assessments and histopathological reports provided the basis for case identification and classification. The author further thanks the laboratory and digital pathology personnel for histological and IHC processing, slide scanning, access to archived diagnostic material, and technical support.

Data Availability

The aggregated data supporting the findings of this study are included in the article and its tables. Additional anonymized data underlying the reported analyses may be made available upon justified request, subject to institutional approval and applicable confidentiality regulations. The full case-level dataset is not publicly available because it contains sensitive clinical and pathological information and is subject to institutional data-protection restrictions. Whole-slide image data are not publicly deposited because of file size, local infrastructure requirements, and institutional restrictions regarding archived diagnostic material; access may be considered after institutional approval.

Institutional Review Board Statement

All procedures performed in this retrospective study involving archived human diagnostic material and anonymized clinicopathological data were conducted in accordance with the ethical standards of the institutional research committees and with the Declaration of Helsinki and its later amendments. The study protocol was approved by the Ethics Committee of Lucian Blaga University of Sibiu (Approval No. 26/12 April 2023) and by the Ethics Committee of the Sibiu Emergency County Clinical Hospital (Approval No. 13165/ 29 May 2023).

Informed Consent Statement

The requirement for individual informed consent was waived by the approving ethics committees because of the retrospective, non-interventional design, the use of archived diagnostic material, and anonymized data analysis.

Consent for publication

Consent for publication was not required because the study used anonymized retrospective data and archived diagnostic material without identifiable patient information.

References

[1] Alaggio R, Amador C, Anagnostopoulos I, Attygalle AD, Araujo IBO, Berti E, Bhagat G, Borges AM, Boyer D, Calaminici M, Chadburn A, Chan JKC, Cheuk W, Chng WJ, Choi JK, Chuang SS, Coupland SE, Czader M, Dave SS, de Jong D, Du MQ, Elenitoba-Johnson KS, Ferry J, Geyer J, Gratzinger D, Guitart J, Gujral S, Harris M, Harrison CJ, Hartmann S, Hochhaus A, Jansen PM, Karube K, Kempf W, Khoury J, Kimura H, Klapper W, Kovach AE, Kumar S, Lazar AJ, Lazzi S, Leoncini L, Leung N, Leventaki V, Li XQ, Lim MS, Liu WP, Louissaint A Jr, Marcogliese A, Medeiros LJ, Michal M, Miranda RN, Mitteldorf C, Montes-Moreno S, Morice W, Nardi V, Naresh KN, Natkunam Y, Ng SB, Oschlies I, Ott G, Parrens M, Pulitzer M, Rajkumar SV, Rawstron AC, Rech K, Rosenwald A, Said J, Sarkozy C, Sayed S, Saygin C, Schuh A, Sewell W, Siebert R, Sohani AR, Tooze R, Traverse-Glehen A, Vega F, Vergier B, Wechalekar AD, Wood B, Xerri L, Xiao W. The 5th edition of the World Health Organization Classification of Haematolymphoid Tumours: Lymphoid Neoplasms. Leukemia, 2022, 36(7):1720–1748. https://doi.org/10.1038/s41375-022-01620-2 PMID: 35732829 PMCID: PMC9214472

[2] Campo E, Jaffe ES, Cook JR, Quintanilla-Martinez L, Swerdlow SH, Anderson KC, Brousset P, Cerroni L, de Leval L, Dirnhofer S, Dogan A, Feldman AL, Fend F, Friedberg JW, Gaulard P, Ghia P, Horwitz SM, King RL, Salles G, San-Miguel J, Seymour JF, Treon SP, Vose JM, Zucca E, Advani R, Ansell S, Au WY, Barrionuevo C, Bergsagel L, Chan WC, Cohen JI, d'Amore F, Davies A, Falini B, Ghobrial IM, Goodlad JR, Gribben JG, Hsi ED, Kahl BS, Kim WS, Kumar S, LaCasce AS, Laurent C, Lenz G, Leonard JP, Link MP, Lopez-Guillermo A, Mateos MV, Macintyre E, Melnick AM, Morschhauser F, Nakamura S, Narbaitz M, Pavlovsky A, Pileri SA, Piris M, Pro B, Rajkumar V, Rosen ST, Sander B, Sehn L, Shipp MA, Smith SM, Staudt LM, Thieblemont C, Tousseyn T, Wilson WH, Yoshino T, Zinzani PL, Dreyling M, Scott DW, Winter JN, Zelenetz AD. The International Consensus Classification of Mature Lymphoid Neoplasms: a report from the Clinical Advisory Committee. Blood, 2022, 140(11):1229–1253. https://doi.org/10.1182/blood.2022015851 PMID: 35653592 PMCID: PMC9479027

[3] Scott DW, Gascoyne RD. The tumour microenvironment in B cell lymphomas. Nat Rev Cancer, 2014, 14(8):517–534. https://doi.org/10.1038/nrc3774 PMID: 25008267

[4] Ng WL, Ansell SM, Mondello P. Insights into the tumor microenvironment of B cell lymphoma. J Exp Clin Cancer Res, 2022, 41(1):362. https://doi.org/10.1186/s13046-022-02579-9 PMID: 36578079 PMCID: PMC9798587

[5] Liu Y, Zhou X, Wang X. Targeting the tumor microenvironment in B-cell lymphoma: challenges and opportunities. J Hematol Oncol, 2021, 14(1):125. https://doi.org/10.1186/s13045-021-01134-x PMID: 34404434 PMCID: PMC8369706

[6] Cioroianu AI, Stinga PI, Sticlaru L, Cioplea MD, Nichita L, Popp C, Staniceanu F. Tumor microenvironment in diffuse large B-cell lymphoma: role and prognosis. Anal Cell Pathol (Amst), 2019, 2019:8586354. https://doi.org/10.1155/2019/8586354 PMID: 31934533 PMCID: PMC6942707

[7] Bankhead P, Loughrey MB, Fernández JA, Dombrowski Y, McArt DG, Dunne PD, McQuaid S, Gray RT, Murray LJ, Coleman HG, James JA, Salto-Tellez M, Hamilton PW. QuPath: open source software for digital pathology image analysis. Sci Rep, 2017, 7(1):16878. https://doi.org/10.1038/s41598-017-17204-5 PMID: 29203879 PMCID: PMC5715110

[8] Cieslak C, Mitteldorf C, Krömer-Olbrisch T, Kempf W, Stadler R. QuPath analysis for CD30+ cutaneous T-cell lymphoma. Am J Dermatopathol, 2023, 45(2):93–98. https://doi.org/10.1097/DAD.0000000000002330 PMID: 36669072

[9] Cristian M, Aşchie M, Deacu M, Boşoteanu M, Bălţătescu GI, Stoica AG, Nicolau AA, Poinăreanu I, Orăşanu CI. Comparison of Ki67 proliferation index in gastrointestinal non-Hodgkin large B-cell lymphomas: the conventional method of evaluation or AI evaluation? Diagnostics (Basel), 2023, 13(17):2775. https://doi.org/10.3390/diagnostics13172775 PMID: 37685312 PMCID: PMC10486605

[10] Cerchietti L. Genetic mechanisms underlying tumor microenvironment composition and function in diffuse large B-cell lymphoma. Blood, 2024, 143(12):1101–1111. https://doi.org/10.1182/blood.2023021002 PMID: 38211334 PMCID: PMC10972714

[11] Koumpis E, Papoudou-Bai A, Papathanasiou K, Kolettas E, Kanavaros P, Hatzimichael E. Unraveling the immune microenvironment in diffuse large B-cell lymphoma: prognostic and potential therapeutic implications. Curr Issues Mol Biol, 2024, 46(7):7048–7064. https://doi.org/10.3390/cimb46070420 PMID: 39057061 PMCID: PMC11276293

[12] Cho Y, Lee J, Han B, Yoon SE, Kim SJ, Kim WS, Cho J. Tumor-infiltrating T lymphocytes evaluated using digital image analysis predict the prognosis of patients with diffuse large B-cell lymphoma. J Pathol Transl Med, 2024, 58(1):12–21. https://doi.org/10.4132/jptm.2023.11.02 PMID: 38229430 PMCID: PMC10792279

[13] Iqbal J, Neppalli VT, Wright G, Dave BJ, Horsman DE, Rosenwald A, Lynch J, Hans CP, Weisenburger DD, Greiner TC, Gascoyne RD, Campo E, Ott G, Müller-Hermelink HK, Delabie J, Jaffe ES, Grogan TM, Connors JM, Vose JM, Armitage JO, Staudt LM, Chan WC. BCL2 expression is a prognostic marker for the activated B-cell-like type of diffuse large B-cell lymphoma. J Clin Oncol, 2006, 24(6):961–968. https://doi.org/10.1200/JCO.2005.03.4264 PMID: 16418494

[14] Tsuyama N, Sakata S, Baba S, Mishima Y, Nishimura N, Ueda K, Yokoyama M, Terui Y, Hatake K, Kitagawa M, Ishizuka N, Tomita N, Takeuchi K. BCL2 expression in DLBCL: reappraisal of immunohistochemistry with new criteria for therapeutic biomarker evaluation. Blood, 2017, 130(4):489–500. https://doi.org/10.1182/blood-2016-12-759621 PMID: 28522442

[15] Vijenthira A, Gong IY, Fox TA, Booth S, Cook G, Fattizzo B, Martín-Moro F, Razanamahery J, Riches JC, Zwicker J, Patell R, Vekemans MC, Scarfò L, Chatzikonstantinou T, Yildiz H, Lattenist R, Mantzaris I, Wood WA, Hicks LK. Outcomes of patients with hematologic malignancies and COVID-19: a systematic review and meta-analysis of 3377 patients. Blood, 2020, 136(25):2881–2892. https://doi.org/10.1182/blood.2020008824 PMID: 33113551 PMCID: PMC7746126

[16] Küçükyurt S, Şahin K, Yılmaz U, Erçalışkan A, Özkan Tekin T, Ortaboz D, Elverdi T, Salihoğlu A, Ar MC, Öngören Ş, Başlar Z, Eşkazan AE. Diagnosis and management of classical Hodgkin lymphoma during the COVID-19 pandemic. Curr Probl Cancer, 2022, 46(6):100913. https://doi.org/10.1016/j.currproblcancer.2022.100913 PMID: 36399974 PMCID: PMC9554335

[17] Ekberg S, Molin D, Pahnke S, Bergström F, Brånvall E, Smedby KE, Wästerlid T. Impact of the COVID-19 pandemic on lymphoma incidence and short-term survival – a Swedish Lymphoma Register Study. Acta Oncol, 2024, 63:164–168. https://doi.org/10.2340/1651-226X.2024.35238 PMID: 38591352 PMCID: PMC11332491

[18] Elliott EK, Hensen R, Haupt LM, Griffiths LR. Global reported impacts of COVID-19 on lymphoma patients and the emerging clinical management approaches in response to the ongoing pandemic. Eur J Haematol, 2023, 110(5):457–469. https://doi.org/10.1111/ejh.13926 PMID: 36656099

[19] Passamonti F, Nicastri E, Di Rocco A, Guarini A, Ibatici A, Luminari S, Mikulska M, Visco C. Management of patients with lymphoma and COVID-19: narrative review and evidence-based practical recommendations. Hematol Oncol, 2023, 41(1):3–15. https://doi.org/10.1002/hon.3086 PMID: 36251481 PMCID: PMC9874581

[20] World Health Organization (WHO). WHO Director-General's opening remarks at the media briefing on COVID-19 – 11 March 2020. WHO, Geneva, Switzerland, 2020. https://www.who.int/news-room/speeches/item/who-director-general-s-opening-remarks-at-the-media-briefing-on-covid-19---11-march-2020

[21] Presidency of Romania. Declaraţia de presă susţinută de Preşedintele României, Klaus Iohannis. Presidency of Romania, Bucharest, Romania, 4 March 2022. https://klausiohannis.presidency.ro/ro/media/sanatate/declaratia-de-presa-sustinuta-de-presedintele-romaniei-klaus-iohannis1646403101

[22] Ilie L. Romanian government to lift COVID restrictions from March 9. Reuters, 8 March 2022. https://www.reuters.com/world/europe/romanian-government-lift-covid-restrictions-march-9-2022-03-08/

[23] Wood WA, Neuberg DS, Thompson JC, Tallman MS, Sekeres MA, Sehn LH, Anderson KC, Goldberg AD, Pennell NA, Niemeyer CM, Tucker E, Hewitt K, Plovnick RM, Hicks LK. Outcomes of patients with hematologic malignancies and COVID-19: a report from the ASH Research Collaborative Data Hub. Blood Adv, 2020, 4(23):5966–5975. https://doi.org/10.1182/bloodadvances.2020003170 PMID: 33278301 PMCID: PMC7724912

[24] Heer E, Ruan Y, Boyne DJ, Jarada TN, Heng D, Henning JW, Morris DM, O'Sullivan DE, Cheung WY, Brenner DR. Impact of the COVID-19 pandemic on cancer diagnoses, stage and survival in Alberta. CMAJ, 2023, 195(23):E804–E812. https://doi.org/10.1503/cmaj.221512 PMID: 37308211 PMCID: PMC10260240

[25] Angelini M, Teglia F, Astolfi L, Casolari G, Boffetta P. Decrease of cancer diagnosis during COVID-19 pandemic: a systematic review and meta-analysis. Eur J Epidemiol, 2023, 38(1):31–38. https://doi.org/10.1007/s10654-022-00946-6 PMID: 36593334 PMCID: PMC9807424

[26] Shah R, Hanna NM, Loo CE, David M, Mafra A, Fink H, McFerran E, Garcia M, Ghodssighassemabadi R, Acharya S, Niyibaga J, Langselius O, Frick C, Lasebikan N, Vignat J, Steinberg J, Hughes S, Kircher CE, Goldie CL, Egger S, Sullivan R, Ginsburg O, Bray F, Caruana M, Hui H, Ilbawi AM, Canfell K, Soerjomataram I. The global impact of the COVID-19 pandemic on delays and disruptions in cancer care services: a systematic review and meta-analysis. Nat Cancer, 2025, 6(1):194–204. https://doi.org/10.1038/s43018-024-00880-4 PMID: 39747650

[27] Monti S, Savage KJ, Kutok JL, Feuerhake F, Kurtin P, Mihm M, Wu B, Pasqualucci L, Neuberg D, Aguiar RC, Dal Cin P, Ladd C, Pinkus GS, Salles G, Harris NL, Dalla-Favera R, Habermann TM, Aster JC, Golub TR, Shipp MA. Molecular profiling of diffuse large B-cell lymphoma identifies robust subtypes including one characterized by host inflammatory response. Blood, 2005, 105(5):1851–1861. https://doi.org/10.1182/blood-2004-07-2947 PMID: 15550490

[28] Lenz G, Wright G, Dave SS, Xiao W, Powell J, Zhao H, Xu W, Tan B, Goldschmidt N, Iqbal J, Vose J, Bast M, Fu K, Weisenburger DD, Greiner TC, Armitage JO, Kyle A, May L, Gascoyne RD, Connors JM, Troen G, Holte H, Kvaloy S, Dierickx D, Verhoef G, Delabie J, Smeland EB, Jares P, Martinez A, Lopez-Guillermo A, Montserrat E, Campo E, Braziel RM, Miller TP, Rimsza LM, Cook JR, Pohlman B, Sweetenham J, Tubbs RR, Fisher RI, Hartmann E, Rosenwald A, Ott G, Muller-Hermelink HK, Wrench D, Lister TA, Jaffe ES, Wilson WH, Chan WC, Staudt LM; Lymphoma/Leukemia Molecular Profiling Project. Stromal gene signatures in large-B-cell lymphomas. N Engl J Med, 2008, 359(22):2313–2323. https://doi.org/10.1056/NEJMoa0802885 PMID: 19038878 PMCID: PMC9103713

[29] Song JY, Nwangwu M, He TF, Zhang W, Meawad H, Bedell V, Murata-Collins J, Skrabek P, Nasr MR, Scott D, Godfrey J,

Lee P, Chan WC, Weisenburger DD, Perry AM, Herrera AF. Low T-cell proportion in the tumor microenvironment is associated with immune escape and poor survival in diffuse large B-cell lymphoma. Haematologica, 2023, 108(8):2167–2177. https://doi.org/10.3324/haematol.2022.282265 PMID: 36632739 PMCID: PMC10388272

[30] Colombo AR, Hav M, Singh M, Xu A, Gamboa A, Lemos T, Gerdtsson E, Chen D, Houldsworth J, Shaknovich R, Aoki T, Chong L, Takata K, Chavez EA, Steidl C, Hicks J, Kuhn P, Siddiqi I, Merchant A. Single-cell spatial analysis of tumor immune architecture in diffuse large B-cell lymphoma. Blood Adv, 2022, 6(16):4675–4690. https://doi.org/10.1182/bloodadvances.2022007493 PMID: 35675517 PMCID: PMC9631676

[31] Wright KT, Weirather JL, Jiang S, Kao KZ, Sigal Y, Giobbie-Hurder A, Shipp MA, Rodig SJ. Diffuse large B-cell lymphomas have spatially defined, tumor immune microenvironments revealed by high-parameter imaging. Blood Adv, 2023, 7(16):4633–4646. https://doi.org/10.1182/bloodadvances.2023009813 PMID: 37196647 PMCID: PMC10448427

[32] Reiss DJ, Nakayama Y, Weng AP, Stokes ME, Sehn L, Steidl C, Scott DW, Huang CC, Gandhi AK. High-plex imaging and cellular neighborhood spatial analysis reveals multiple immune escape and suppression patterns in diffuse large B-cell lymphoma. Leukemia, 2024, 38(5):1164–1168. https://doi.org/10.1038/s41375-024-02239-1 PMID: 38575670 PMCID: PMC11073958

[33] Han B, Yim J, Lim S, Na S, Lee C, Kim TM, Paik JH, Kim S, Jeon YK. Prognostic impact of the immunoscore based on whole-slide image analysis of CD3+ tumor-infiltrating lymphocytes in diffuse large B-cell lymphoma. Mod Pathol, 2023, 36(9):100224. https://doi.org/10.1016/j.modpat.2023.100224 PMID: 37257823

[34] Autio M, Leivonen SK, Meriranta L, Karjalainen-Lindsberg ML, Pellinen T, Leppä S. Spatial analysis of the tumor microenvironment in diffuse large B-cell lymphoma reveals clinically relevant cell interactions and recurrent cellular neighborhoods. Cancer Immunol Res, 2025, 13(10):1674–1686. https://doi.org/10.1158/2326-6066.CIR-24-1163 PMID: 40772779 PMCID: PMC12485370

[35] Coutinho R, Clear AJ, Mazzola E, Owen A, Greaves P, Wilson A, Matthews J, Lee A, Alvarez R, da Silva MG, Cabeçadas J, Neuberg D, Calaminici M, Gribben JG. Revisiting the immune microenvironment of diffuse large B-cell lymphoma using a tissue microarray and immunohistochemistry: robust semi-automated analysis reveals CD3 and FoxP3 as potential predictors of response to R-CHOP. Haematologica, 2015, 100(3):363–369. https://doi.org/10.3324/haematol.2014.110189 PMID: 25425693 PMCID: PMC4349275

[36] Autio M, Leivonen SK, Brück O, Mustjoki S, Mészáros Jørgensen J, Karjalainen-Lindsberg ML, Beiske K, Holte H, Pellinen T, Leppä S. Immune cell constitution in the tumor microenvironment predicts the outcome in diffuse large B-cell lymphoma. Haematologica, 2021, 106(3):718–729. https://doi.org/10.3324/haematol.2019.243626 PMID: 32079690 PMCID: PMC7927991

[37] Zhang S, Asquith B, Szydlo R, Tregoning JS, Pollock KM. Peripheral T cell lymphopenia in COVID-19: potential mechanisms and impact. Immunother Adv, 2021, 1(1):ltab015. https://doi.org/10.1093/immadv/ltab015 PMID: 35965490 PMCID: PMC9364037

[38] André S, Picard M, Cezar R, Roux-Dalvai F, Alleaume-Butaux A, Soundaramourty C, Cruz AS, Mendes-Frias A, Gotti C, Leclercq M, Nicolas A, Tauzin A, Carvalho A, Capela C, Pedrosa J, Castro AG, Kundura L, Loubet P, Sotto A, Muller L, Lefrant JY, Roger C, Claret PG, Duvnjak S, Tran TA, Racine G, Zghidi-Abouzid O, Nioche P, Silvestre R, Droit A, Mammano F, Corbeau P, Estaquier J. T cell apoptosis characterizes severe Covid-19 disease. Cell Death Differ, 2022, 29(8):1486–1499. https://doi.org/10.1038/s41418-022-00936-x PMID: 35066575 PMCID: PMC8782710

[39] Turner JS, O'Halloran JA, Kalaidina E, Kim W, Schmitz AJ, Zhou JQ, Lei T, Thapa M, Chen RE, Case JB, Amanat F, Rauseo AM, Haile A, Xie X, Klebert MK, Suessen T, Middleton WD, Shi PY, Krammer F, Teefey SA, Diamond MS, Presti RM, Ellebedy AH. SARS-CoV-2 mRNA vaccines induce persistent human germinal centre responses. Nature, 2021, 596(7870):109–113. https://doi.org/10.1038/s41586-021-03738-2 PMID: 34182569 PMCID: PMC8935394

[40] Cohen D, Hazut Krauthammer S, Cohen YC, Perry C, Avivi I, Herishanu Y, Even-Sapir E. Correlation between BNT162b2 mRNA Covid-19 vaccine-associated hypermetabolic lymph-adenopathy and humoral immunity in patients with hematologic malignancy. Eur J Nucl Med Mol Imaging, 2021, 48(11):3540–3549. https://doi.org/10.1007/s00259-021-05389-x PMID: 33966088 PMCID: PMC8106512

[41] Menter T, Zinner CP, Berger CT, Went P, Tzankov A. Case Report: Gene expression profiling of COVID-19 vaccination-related lymphadenopathies reveals evidence of a dominantly extrafollicular immune response. Front Immunol, 2023, 14:1285168. https://doi.org/10.3389/fimmu.2023.1285168 PMID: 38035070 PMCID: PMC10682704

[42] Claaß LV, Mayr P, Paschold L, Weber T, Terziev D, Jehs B, Brill R, Dober J, Märkl B, Wickenhauser C, Czapiewski P, Trepel M, Claus R, Binder M. No association of malignant B-cell non-Hodgkin lymphomas with ipsilateral SARS-CoV-2 vaccination. Cancer Med, 2023, 12(8):9313–9321. https://doi.org/10.1002/cam4.5687 PMID: 36775947 PMCID: PMC10166887

[43] Roh J, Cho H, Yoon DH, Hong JY, Lee AN, Eom HS, Lee H, Park WS, Han JH, Jeong SH, Park JS, Pak HK, Kim SW, Kim SY, Suh C, Huh J, Park CS. Quantitative analysis of tumor-specific BCL2 expression in DLBCL: refinement of prognostic relevance of BCL2. Sci Rep, 2020, 10(1):10680. https://doi.org/10.1038/s41598-020-67738-4 PMID: 32606309 PMCID: PMC7326926

Corresponding author

Paul-Cătălin Toboltoc, MD, PhD Student, Department of Pathology, Sibiu Emergency County Clinical Hospital, 2–4 Corneliu Coposu Avenue, 550245 Sibiu, Sibiu County, Romania; Phone +40269–215 050 int. 147, e-mail: paul.toboltoc@gmail.com

Received: May 10, 2026

Accepted: October 26, 2026